

See discussions, stats, and author profiles for this publication at: <https://www.researchgate.net/publication/6236031>

# Ab Initio Molecular Dynamics of Excited-State Intramolecular Proton Transfer Using Multireference Perturbation Theory †

ARTICLE *in* THE JOURNAL OF PHYSICAL CHEMISTRY A · DECEMBER 2007

Impact Factor: 2.69 · DOI: 10.1021/jp072027b · Source: PubMed

---

CITATIONS

53

---

READS

64

3 AUTHORS, INCLUDING:



**Joshua D Coe**

Los Alamos National Laboratory

30 PUBLICATIONS 482 CITATIONS

SEE PROFILE



**Todd J. Martinez**

Stanford University

239 PUBLICATIONS 7,863 CITATIONS

SEE PROFILE

# Ab Initio Molecular Dynamics of Excited-State Intramolecular Proton Transfer Using Multireference Perturbation Theory<sup>†</sup>

Joshua D. Coe, Benjamin G. Levine, and Todd J. Martínez\*

Department of Chemistry, Beckman Institute, and Frederick Seitz Materials Research Laboratory,  
University of Illinois, Urbana, Illinois 61801

Received: March 13, 2007; In Final Form: May 18, 2007

We present the first calculations of excited-state dynamics using ab initio molecular dynamics with a multireference perturbation theory description of the electronic structure. The new AIMS-CASPT2 method is applied to a paradigmatic excited-state intramolecular proton-transfer reaction in methyl salicylate, and the results are compared with previous ultrafast spectroscopic experiments. Agreement of AIMS-CASPT2 and experimental results is quantitative. The results demonstrate that the lack of an observed isotope effect in the reaction is due to multidimensionality of the reaction coordinate, which largely involves heavy-atom bond alternation instead of proton transfer. Using the dynamics results as a guide, we also characterize relevant minima on the ground and first singlet excited state using CASPT2 electronic structure theory. We further locate an  $S_1/S_0$  minimal energy conical intersection, whose presence explains experimental observations of a sharp decrease in fluorescence quantum yield at excitation energies more than 1300  $\text{cm}^{-1}$  above the excited-state origin.

## Introduction

Ab initio molecular dynamics (AIMD) methods have proven to be an exceptionally powerful tool in chemical simulation, especially for reactions involving electronically excited states<sup>1–6</sup> where it is difficult to devise sufficiently flexible empirical force fields. AIMD methods allow arbitrary bond rearrangement because they solve the electronic Schrödinger equation at each time step in order to determine the forces acting on the atoms. However, this also implies that AIMD methods are computationally challenging. Consequently, AIMD methods for electronically excited states have often used<sup>1–3</sup> the complete active space self-consistent field (CASSCF) method,<sup>7</sup> which provides flexibility sufficient to describe bond rearrangement and multiple electronic states (often referred to as “static” electron correlation) but is ill-suited for detailed description of dynamic electron correlation effects. Dynamic electron correlation is well-known to play a key role in quantitative measures relevant to chemical reactions such as barrier heights and vertical excitation energies. We have previously reported ab initio dynamics using the equation of motion coupled cluster (EOM-CCSD) approach,<sup>8</sup> which is a partial solution to the problem. However, EOM-CCSD can only work well when the underlying CCSD method provides a good description of the ground electronic state. This can cause problems when bonds are being broken or formed and the ground electronic state has significant multireference character. Multireference perturbation theory approaches, such as CASPT2,<sup>9</sup> provide a cost-effective means of including dynamic correlation effects while simultaneously describing bond rearrangement. The accuracy of these methods, as judged by comparison of computed excitation energies and measured absorption spectra, is often better than 0.5 eV.<sup>9</sup> The absence of analytic energy gradients has prevented the use of CASPT2 in AIMD methods. However, the methodology for analytic gradients has recently been developed and implemented.<sup>10</sup> This

breakthrough sets the stage for AIMD calculations on excited electronic states with full account of both static and dynamic electron correlation. In this Article, we report on the first such calculations, using excited-state intramolecular proton transfer (ESIPT) in methyl salicylate (MS) as an example. The results are compared directly to ultrafast spectroscopic experiments, with quantitative agreement.

Excited-state proton transfer is the fundamental basis of photoacidity and is a key step in photoactive proteins such as green fluorescent protein<sup>11,12</sup> (GFP). The intramolecular case provides an important testing ground for understanding this process, as diffusion control need not be considered. A number of experiments have probed excited-state intramolecular proton transfer (ESIPT) in gas phase,<sup>13–16</sup> cluster,<sup>17</sup> and condensed phase<sup>18</sup> environments. As shown by previous theoretical studies,<sup>19–21</sup> the ESIPT process is, in many cases, better described as strongly coupled electron and proton transfer, that is, H atom transfer. The time scale for ESIPT makes it one of the fastest chemical reactions known, with experimental estimates of the H atom transfer time being as fast as 50 fs. Curiously, H/D isotopic substitution of the transferring H atom has little effect on the transfer time. It has been suggested on the basis of static calculations of potential energy surfaces (PESs) that this insensitivity to isotopic substitution comes about because the reaction coordinate is strongly multidimensional.<sup>13,21</sup>

Previous experimental work on MS (see Scheme 1) has focused on three features: dual fluorescence, proton transfer, and the excess energy dependence of the fluorescence decay rate. The first of these, observation of fluorescence bands at both 330 and 440 nm, appears largely to have been resolved on the basis of two distinct ground-state rotamers (only one of which undergoes ESIPT, leading to a large Stokes shift and thus the redder of the two fluorescence bands). Time-resolved experiments<sup>13</sup> predicted an upper bound of 60 fs for ESIPT and found no evidence of an isotope effect. The fluorescence decay rate showed little dependence on excitation energy up to an

<sup>†</sup> Part of the “Thom H. Dunning, Jr., Festschrift”.

enol

keto

The traditional description of ESIPT assigned a central role to the donor–hydrogen stretch. Attention thus was largely restricted to a one-dimensional reaction coordinate, highlighting its barrier height and tunneling correction.<sup>14</sup> As experimental time resolution increased, it was observed that recovery rates (usually of product fluorescence) tracked laser cross correlations at the pico-<sup>23</sup> and then the femtosecond<sup>13</sup> time scale. Thus, it became clear that ESIPT could be effectively barrierless even for isolated molecules at low temperature. In parallel with increasingly accurate experiments, it was realized<sup>24,25</sup> that electronic structure methods which do not include dynamic electron correlation erroneously predict large proton-transfer barriers on the bright  $\pi\pi^*$  state. When resonance Raman experiments found no enhancement of the donor–hydrogen stretch in *o*-hydroxyacetophenone,<sup>26</sup> attention turned to the promoting role of spectator modes. Transient absorption studies<sup>16,27–29</sup> since have sharpened the focus specifically onto low-frequency (backbone) vibrations. The present results lend additional clarity and confirmation to this evolving picture of particle exchange regulated (or “gated”) by global molecular rearrangement.

## Methods

The AIMS method has been discussed in the literature, and the interested reader is referred there for methodological details.<sup>31</sup> In the present work, the zeroth-order electronic structure problem for the ground and excited states is solved using a complete active space self-consistent field (CASSCF) method with two electrons in two orbitals. We have previously discussed the challenges of describing ESIPT using CASSCF for the paradigmatic case of malonaldehyde.<sup>1</sup> Briefly, increasing the size of the active space increases the proton-transfer barrier on the excited state. This barrier is subsequently decreased (and even completely erased) when dynamic correlation effects are included using either perturbative (CASPT2) or variational

The nuclear wave function in AIMS for electronic state I (projected onto position states  $\mathbf{X}$ ) is represented as a sum of  $N$  Gaussians  $\chi_I$  having complex time-dependent coefficients  $c_I$  and parametrized by mean positions  $\mathbf{R}$ , momenta  $\mathbf{P}$ , fixed widths  $\alpha$ , and phase  $\gamma$

$$\langle \mathbf{X}|I \rangle = \Psi_{\text{AIMS}}^{(\text{I})}(\mathbf{R}, \mathbf{r}, t) = \sum_i^{N_I(t)} c_j(t) \chi_j(\mathbf{R}, t; \bar{\mathbf{R}}_j, \bar{\mathbf{P}}_j, \alpha, \gamma_j) \varphi_j^{(\text{I})}(\mathbf{r}; \bar{\mathbf{R}}_j) \quad (1)$$

$$\chi_j = e^{iyt} \prod_{\rho=1}^{3N} e^{-\alpha_\rho (R_\rho - \bar{R}_\rho)^2 + i\bar{P}_\rho (R_\rho - \bar{R}_\rho)} \quad (2)$$

where  $\rho$  labels the individual Cartesian coordinates of the nuclei. The coefficients  $c_j$  are propagated with the time-dependent Schrödinger equation, while the basis function parameters  $\bar{\mathbf{R}}$  and  $\bar{\mathbf{P}}$  evolve classically and the phase semiclassically (as the time integral of the Lagrangian). The widths are chosen as discussed previously,<sup>31</sup> and the specific values used here are 30 and 6 bohr<sup>-2</sup> for C/O and H atoms, respectively. Initial conditions for the phase space centers of the TBFs are chosen by random sampling from the Wigner distribution<sup>37</sup> corresponding to the ground vibrational state on  $S_0$  in the harmonic

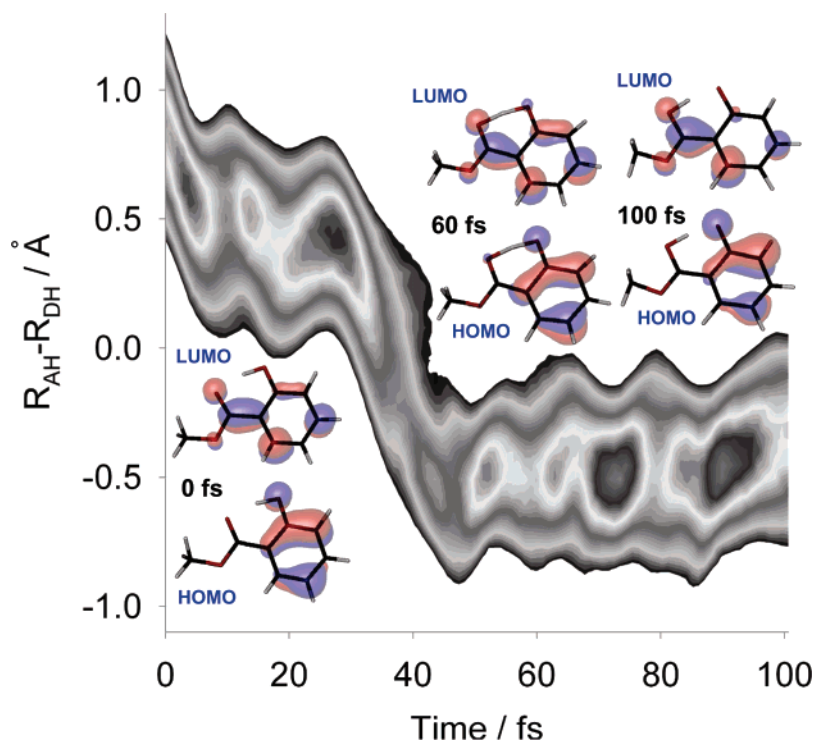


**Figure 1.** Evolution of the AIMS nuclear density along the hydrogen-transfer coordinate  $R_{\text{AH}}-R_{\text{DH}}$ . Representative molecular geometries at different points in the dynamics are also shown, along with the natural orbitals of the state-averaged density matrix defining the active space (labeled as HOMO and LUMO according to their occupancy on  $S_0$ ). The  $S_1$  electronic wave function is dominantly represented as having a single electron in each of the HOMO and LUMO orbitals (see Table 1).

approximation. The  $S_0$  minimum geometry and frequencies used to generate the Wigner distribution are obtained using B3LYP density functional theory with a 6-31G\* basis set.<sup>38</sup> The Wigner-sampled initial TBFs are then associated with the bright excited electronic state,  $S_1$  in MS. This approximates the nuclear wave function found on the excited electronic state after an ultrashort laser pulse near resonance with the  $S_0 \rightarrow S_1$  electronic transition in low-temperature, isolated conditions. Five independent trajectory basis functions (for each of the two isotopes of MS) are used in the present simulations, and the results shown are averages over these five trajectories.

It will prove convenient to visualize reduced AIMS wave function probability densities along various coordinates important to ESPT. One generally runs a number of AIMS simulations (“runs”) corresponding to different initial conditions, and the results are incoherently averaged over the  $N_{\text{sim}}$  separate runs. Distinguishing wave function ingredients for different runs by parenthesized superscripts and specifying to the particular case where all TBFs are associated with the same electronic state, the expectation value of an operator  $\hat{O}$  at time  $t$  is computed as

$$\langle O \rangle = \frac{1}{N_{\text{sim}}} \sum_{i=1}^{N_{\text{sim}}} \sum_{j,k=1}^{N_f(t)} (c_j^{(i)}(t))^* c_k^{(i)}(t) \langle \chi_j^{(i)}(t) | \hat{O} | \chi_k^{(i)}(t) \rangle \quad (3)$$

where the wave function in each run is normalized. The positions and momenta are generally written in Cartesian coordinates, but it is more instructive to plot the probability density corresponding to the AIMS wave function in internal coordinates. Although direct transformation of the wave function into internal coordinates is possible in principle, the Gaussian form of the basis functions generally is not preserved when one transforms to internal coordinates. The integrals which result often have no analytic form and require numerical quadrature.

Thus, it is convenient to avoid transforming the wave function and instead evaluate the required integrals directly by Monte Carlo.

Consider, for simplicity, a single internal coordinate. The reduced density as a function of this coordinate is the desired quantity. This reduced density can be expressed as the following integral

$$\rho(\tilde{x})d\tilde{x} = \frac{\int d\mathbf{R} \delta(f(\mathbf{R}) - \tilde{x}) \psi^*(\mathbf{R}) \psi(\mathbf{R})}{\int d\mathbf{R} \psi^*(\mathbf{R}) \psi(\mathbf{R})} \quad (4)$$

The wave functions are expressed in the Cartesian coordinate system,  $\mathbf{R}$ , while the desired density is expressed in an arbitrary coordinate system,  $\tilde{x}$ . The function  $f(\mathbf{R})$  is the coordinate transformation function, returning the value of the  $\tilde{x}$  coordinate, given the values of the  $\mathbf{R}$  coordinates. The presence of the delta function in the numerator then ensures that integration is performed over the remaining spatial coordinates. Since the AIMS wave function is always normalized, the denominator will be ignored in what follows. As a numerical convenience, the delta function in the numerator is replaced by a series of window functions with constant width, that is, “boxes” in a histogram. Specifically, the window functions are

$$w_i(y) = \begin{cases} 1 & \text{if } y_{i-1} < y < y_{i+1} \\ 0 & \text{otherwise} \end{cases} \quad (5)$$

where  $y_1$  and  $y_{N_{\text{Box}}}$  are the smallest and largest values of the internal coordinate (which should be small/large enough to ensure that the wave function is always zero outside of the chosen range). With these clarifications, we can write

$$\rho_i(\tilde{x})\Delta\tilde{x} = \int d\mathbf{R} w_i(f(\mathbf{R}) - \tilde{x}) \psi^*(\mathbf{R}) \psi(\mathbf{R}) \quad (6)$$



where  $\Delta\tilde{x}$  is the box width. The required integrals are computed simultaneously using the same Monte Carlo sampling

$$\rho_i(\tilde{x})\Delta\tilde{x} = \frac{1}{N_{\text{MCSamples}}} \sum_{j=1}^{N_{\text{MCSamples}}} w_i(f(\mathbf{R}_j) - \tilde{x})\psi^*(\mathbf{R}_j)\psi(\mathbf{R}_j) \quad (7)$$

Uniform sampling of the  $\mathbf{R}$  coordinates yields a very slowly convergent procedure. Thus, we importance sample the density with the following importance sampling function

$$\rho_{\text{imp}}(\mathbf{R}) = \sum_i^{N_{\text{bf}}} |c_i|^2 |\chi_i(\mathbf{R})|^2 = \sum_i^{N_{\text{bf}}} n_i |\chi_i(\mathbf{R})|^2 \quad (8)$$

where  $n_i$  is the population for the  $i$ th trajectory basis function. Since the trajectory basis functions are normalized

$$\int \rho_{\text{imp}}(\mathbf{R}) d\mathbf{R} = \sum_i n_i \quad (9)$$

It should be clear that the density corresponding to each TBF is positive definite. As long as the  $n_i$  are all positive, the importance sampling function is therefore positive definite. We first choose one of the TBFs according to the distribution specified by  $n_i$ . Then, a point is chosen from the  $i$ th trajectory by sampling each of the Cartesian coordinates from the appropriate Gaussian distribution. Finally, we compute the value of the internal coordinate  $\tilde{x}$ , increment the number of samples, and add the computed density to the box containing  $\tilde{x}$ . In mathematical terms

$$\rho_i(\tilde{x})\Delta\tilde{x} = \frac{1}{N_{\text{MCSamples}}} \sum_{j=1}^{N_{\text{MCSamples}}} \frac{w_i(f(\mathbf{R}_j) - \tilde{x})\psi^*(\mathbf{R}_j)\psi(\mathbf{R}_j)}{\rho_{\text{imp}}(\mathbf{R}_j)} \quad (10)$$

where  $\mathbf{R}_j$  is sampled from  $\rho_{\text{imp}}(\mathbf{R})$ .

## Results and Discussion

In agreement with experimental results, the AIMS dynamics simulations predict ultrafast ESIPT upon electronic excitation to the lowest  $\pi\pi^*$  state ( $S_1$ ) in MS. In Figure 1, we plot the time evolution of the reduced AIMS nuclear density along the coordinate describing the difference in bond lengths between the transferring H atom and  $O_2$  ( $R_{\text{AH}}$ ) and between the transferring H atom and  $O_1$  ( $R_{\text{DH}}$ ). We are using the atom numbering given in Scheme 1, and we refer to  $O_2$  and  $O_1$  as the “acceptor” and “donor” O atoms in what follows. The change from positive to negative values in Figure 1 corresponds to transfer of the H atom from donor to acceptor. H atom transfer is complete within  $\sim 40$  fs. In addition to the AIMS nuclear density, Figure 1 presents snapshots of the two active space (state-averaged) orbitals at different points in the simulation. The dominant configuration representing  $S_1$  throughout the course of the simulation is a single excitation from HOMO to LUMO, as reflected by the CI coefficients given in Table 1. Electron density in the LUMO orbital is concentrated, in part, along the bond connecting benzene and methoxy groups, a portent of the ensuing bond alternation favorable to tautomerization. The HOMO and LUMO orbitals contain little contribution from the transferring hydrogen atom. Therefore, from an electronic perspective, the transferring hydrogen is a spectator in the reaction. This is the fundamental reason for the lack of an observed isotope effect when the transferring hydrogen atom is replaced by deuterium. We have carried out AIMS simulations

**TABLE 1: Configuration Interaction Coefficients for a SA-2-CAS(2/2)/6-31G\* Wave Function at Three Points along a Representative Trajectory Shown in Figure 1<sup>a</sup>**

	20>	11>	02>
0 fs			
$S_0$	0.971	-0.234	0.000
$S_1$	-0.234	0.972	0.000
60 fs			
$S_0$	0.975	-0.212	-0.068
$S_1$	0.211	0.976	-0.015
100 fs			
$S_0$	0.913	-0.407	0.000
$S_1$	-0.407	0.914	0.000

<sup>a</sup> Configurations are spin-adapted with the orbital occupancy given in the top row as  $|\phi_{\text{HOMO}}\phi_{\text{LUMO}}\rangle$ . Thus, the second column gives CI coefficients for configurations having a doubly occupied HOMO and an empty LUMO.

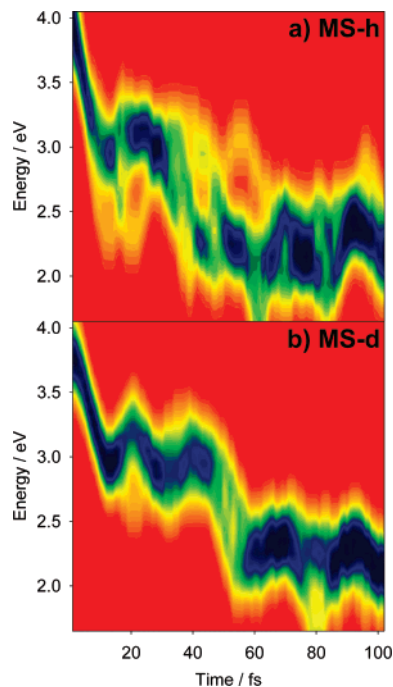


**Figure 2.** Time- and energy-resolved fluorescence spectra for MS-h (top) and MS-d (bottom). Evolution of the Stokes shift is clearly visible at  $\sim 35$  (protonated) and  $\sim 50$  fs (deuterated). Note that the cubic dependence on emission frequency has been suppressed to enhance detail in the low-energy region, as discussed in the text.

for two isotopomers of MS, fully protonated (MS-h) and with the transferring hydrogen atom replaced by deuterium (MS-d). As shown below, the transfer time is negligibly effected by this isotopic substitution.

ESIPT generally is accompanied by a large Stokes shift separating absorption and emission maxima. We have used the AIMS data to generate a fully time- and energy-resolved fluorescence spectrum, shown in Figures 2a (MS-h, top) and b (MS-d, bottom). For each trajectory basis function, the fluorescence intensity  $I$  as a function of emission energy gap  $\Delta E$  at time  $t$  was taken to be proportional to the square of the  $S_0/S_1$  transition dipole moment at the center of the TBF

$$I(\Delta E, t) \propto \sum_{i=1}^{N_{S_1}(t)} c_i^*(t) c_i(t) |\mu_{S_0/S_1}(\bar{\mathbf{R}}_i(t))|^2 \delta(\Delta E - V_{S_1}(\bar{\mathbf{R}}_i(t)) + V_{S_0}(\bar{\mathbf{R}}_i(t))) \quad (11)$$

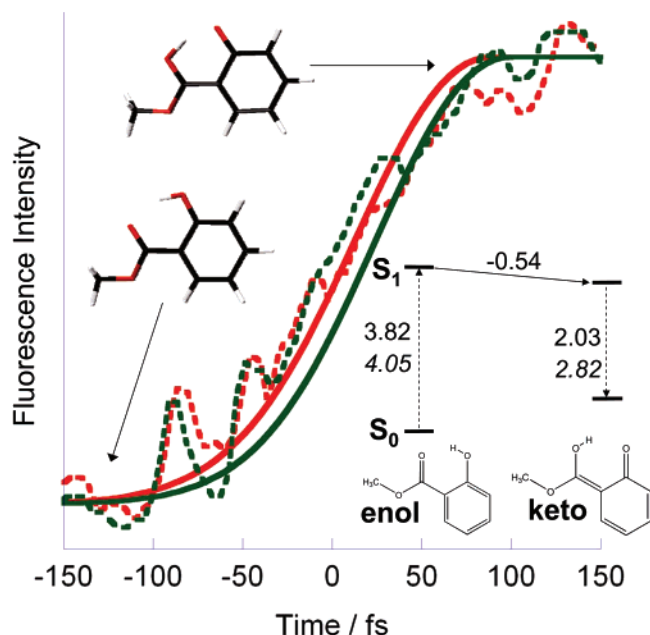


**Figure 3.** Experimental (dotted lines) and predicted (solid lines) time-resolved fluorescence transients for MS, where the transferring atom is H (red) or D (green). Experimental results are from ref 13. The inset (lower right) shows the experimental (italics) and CASPT2 absorption and emission energies in electronvolts.

The cubic dependence on emission frequency, representing the photon density of states, is omitted in order to emphasize the more interesting low-energy region of the spectrum. The final fluorescence intensity is obtained by incoherently averaging over all simulations for a given isotopomer. We calculated the fluorescence intensity at 1 fs intervals, and the resulting data were convoluted in energy with a Gaussian having a full-width at half-maximum (fwhm) of 0.5 eV. The extent of energy broadening is meant to partially compensate for the small size of our nuclear basis sets and does not reflect purely physical limitations on a comparable laboratory measurement. The most suitable experimental counterpart to Figure 2 (after appropriate accounting for the photon density of states) is two-dimensional fluorescence upconversion,<sup>39</sup> which (to our knowledge) has yet to be reported for methyl salicylate. Development of the Stokes shift is clearly evident during the 30–40 fs (MS-h) and 45–55 fs (MS-d) intervals. Superimposed upon the Stokes shift are oscillations whose frequencies vary slightly for the different isotopomers. Casual examination of these variations would assign periods of roughly 20 and 25 fs, respectively, to the deuterated and protonated forms, suggesting excitation in a mode mildly effected by isotopic exchange but strongly coupled to electronic excitation and particle transfer. The observed periods of 20–25 fs correspond to a frequency range of  $\approx 1300$ – $1700$   $\text{cm}^{-1}$ , and inspection of the CASPT2 normal modes calculated at the  $S_0$  minimum indicates several vibrations in this frequency range with substantial C–O stretching and bond alternation components, which will be seen to be important below.

Previous experiments measured the progress of the reaction by monitoring the time-resolved fluorescence at the wavelength of the emission maximum. The emission maximum as computed with the SA-2-CAS(2/2)-PT2 electronic structure method used in our AIMS simulations falls at  $\sim 2.3$  eV (the experimental value is 2.82 eV). Predicted values (from CASPT2) for absorption and emission maxima are shown in the inset of Figure 3. Monitoring the fluorescence intensity at the emission maximum gives the fluorescence transient, which must then be

convoluted in time to account for the finite temporal duration of the pump and probe pulses. The data shown in Figure 3 result from time convolution of the fluorescence intensity at 2.3 eV in the time-energy fluorescence plot shown in Figure 2. The fwhm of the Gaussian used for the time convolution is 140 fs, corresponding to the experimentally measured cross correlation of the pump and probe pulses.<sup>13</sup> The resulting curve is insensitive to the degree of energy broadening in Figure 2, apart from a possible (small) shift in the maximum of the emission spectrum. Agreement between the fluorescence intensity predicted by AIMS (solid lines) and measured values<sup>13</sup> (dashed lines) is quantitative without the use of any adjustable parameters. Both the AIMS simulations and the experiments show an insignificant isotope effect, as seen by comparison of the fluorescence signal in the case where the transferring H atom is a proton (red lines) or a deuteron (green lines). Interestingly, the experimental traces shown in Figure 3 have superimposed oscillations with a periodicity of 20–42 fs. These may be related to the oscillations (periodicity of 20–25 fs) observed in Figure 2 (before time convolution).

As expected from the structures shown for enol and keto forms in Scheme 1, we find bond alternation to also be an important coordinate in the early time dynamics. In order to further clarify its promoting role, we have computed a two-dimensional representation of the PES for ESIPT in MS, shown in Figure 4. The axes correspond to the  $R_{\text{AH}}-R_{\text{DH}}$  coordinate describing H atom transfer and a bond alternation coordinate dominated by the C–O bond distances but also including additional contributions from other backbone bond lengths. The black line in Figure 4 shows where the  $S_0/S_1$  energy gap falls to 2.6 eV and represents an approximate dividing surface for the time-resolved fluorescence experiment. The white arrow gives a schematic depiction of the reaction dynamics, showing that more than half of the reaction pathway is dominated by heavy-atom motion in the form of bond alternation. This explains the observed insensitivity of fluorescence measurements to isotope labeling of the transferring H atom.

In order to confirm that the pathway predicted by the PES shown in Figure 4 was actually relevant to dynamical evolution, we generated two-dimensional reduced representations of the AIMS density in the manner described above. Snapshots of the AIMS wavepacket-reduced probability density are pictured in Figure 5 in 12 fs intervals from 0 to 48 fs. To simplify the representation of the density, the bond alternation coordinate was chosen to be the bond length between  $C_7$  and the acceptor oxygen atom ( $O_2$ ). The net change in this bond length upon moving from enol to keto was twice that of any other bond and five times that of most; therefore, it was judged to provide a reasonable approximation to the full bond rearrangement along the axis in Figure 4. Because we did not include all coordinates here, there was an apparent proton-transfer barrier for all values of the bond alternation. However, the L-shaped form of the PES was largely retained. The AIMS densities clearly evolved along the approximate bond alternation axis before passing through the narrow valley to the keto product.

Using the dynamics results as a starting point, we have further characterized the relevant stationary points and verified the resulting picture using CASPT2 wave functions with larger active spaces. Minimization from the Franck–Condon region on  $S_1$  led to an excited-state local minimum representing a “looser” enol form. This geometry is shown along with the  $S_0$  minimum in Figure 6. Frequency analysis at the CASPT2 level revealed this enol form to be a true minimum on  $S_1$ . The benzenoid character of the ring at the  $S_0$  minimum was destroyed

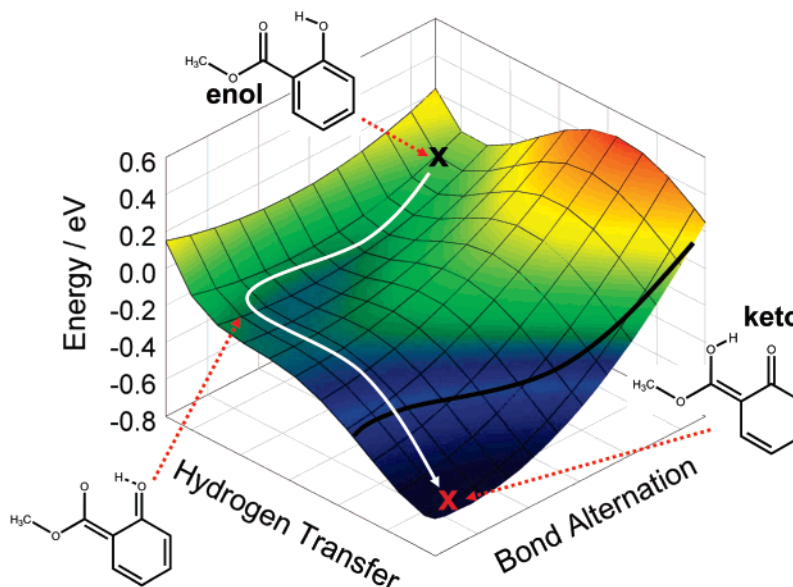


**Figure 4.** Two-dimensional representation of the CAS(2/2)-PT2 reaction surface for ESIPT in MS. The most important coordinates in the dynamics are bond alternation and hydrogen transfer. Immediately after excitation (Franck–Condon point is denoted with a black x), the barrier to H atom transfer is large, but after relaxation along the bond alternation coordinate, this transfer becomes barrierless. Thus, the bond alternation “gates” H atom transfer. No isotope effect is observed because most of the reaction coordinate involves skeletal rearrangement in the form of bond alternation. The dark black line denotes the reaction-dividing surface as measured by fluorescence, chosen to coincide with an  $S_0/S_1$  energy gap of 2.6 eV.

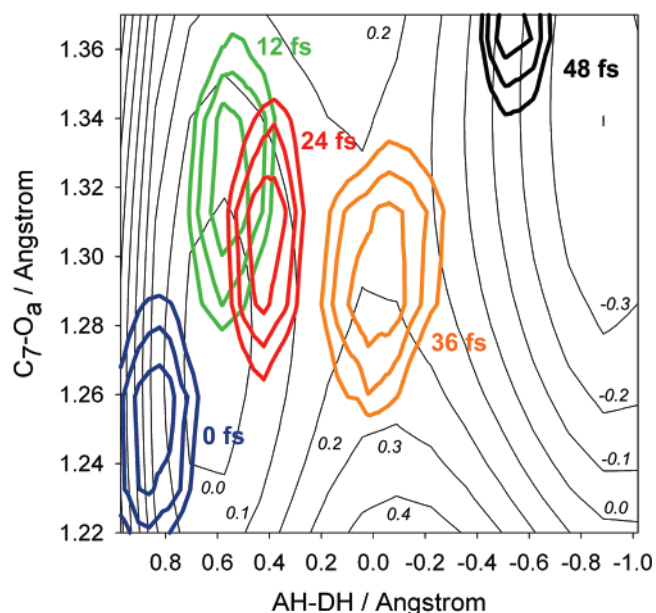


**Figure 5.** Two-dimensional reduced representation of the AIMS wavepacket probability density evolving on the CASPT2  $S_1$  potential surface. The hydrogen-transfer coordinate ( $x$  axis) is plotted against bond alternation, here represented by the one bond showing the largest change ( $+0.1$  Å) in movement from enol to keto. The “gating” effect of changes in backbone bond lengths is evidenced by the wavepacket’s being funneled through the valley connecting the reactant and product. Potential energy surface contour values are given in electronvolts (the zero of energy is taken to be the  $S_1$  energy at the Franck–Condon point), and wave function contours represent 0.85–0.95% density values.

in this enol  $S_1$  minimum by significant extension of the  $C_1$ – $C_2$  and  $C_4$ – $C_5$  bonds, and the bond alternation pattern of the chelate moiety was clearly in the process of reversal. This minimum was briefly accessed in the dynamics, as seen in Figure 2, where the development of the Stokes shift lingered briefly ( $\approx 1$  vibrational period for MS-h,  $\approx 2$  periods for MS-d) at an  $S_0/S_1$

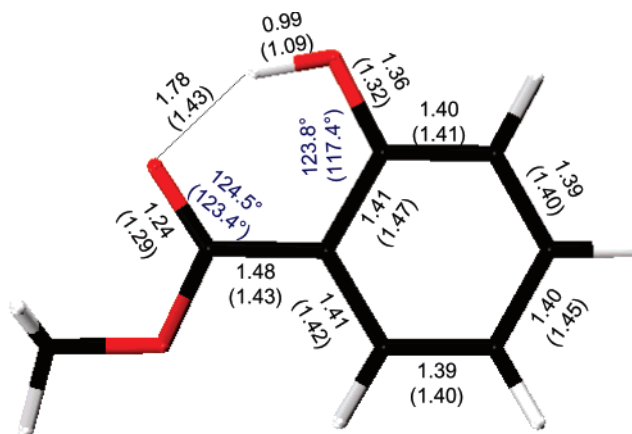


**Figure 6.** Selected bond lengths (angstroms) and angles (degrees) of the enol minimum for methyl salicylate on  $S_0$  and  $S_1$  (in parentheses). Both  $S_0$  and  $S_1$  minima are determined with SA-2-CAS(2/2)-PT2/6-31G\*.

gap of roughly 3 eV, in good agreement with the energy gap at the  $S_1$  local enol minimum (3.03 eV). The wavepacket thus paused on this energy “shelf” before continuing its descent along the reaction path to the global  $S_1$  keto minimum. The decrease in energy gap upon moving to the enol  $S_1$  minimum from the FC region (0.33 eV) matches well with the experimentally reported shift between vertical and adiabatic excitation energies (0.33 eV).<sup>40</sup> This point is discussed further below.

We also found a second  $S_1$  minimum which lies a further 0.2 eV below the enol minimum. This global  $S_1$  minimum is a keto configuration whose bond alternation pattern strongly resembles a proton-transfer transition state in its near-symmetry. The geometry of this global  $S_1$  minimum is shown in Figure 7. Here, the molecular backbone is no longer planar, with  $C_2C_7O_2H$  and  $C_3C_2C_7O_2$  dihedral angles respectively twisted  $15^\circ$  into and out of the plane. The predicted energy gap at this keto geometry is smaller than expected, 2.03 eV compared to the experimental



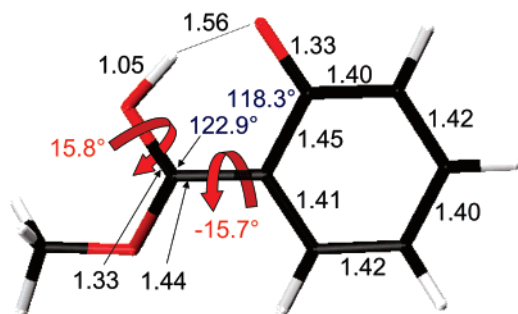


**Figure 7.** Key geometric parameters (bond lengths in angstroms and angles in degrees) of the methyl salicylate keto minimum on  $S_1$ , determined with SA-2-CAS(2/2)-PT2/6-31G\*.

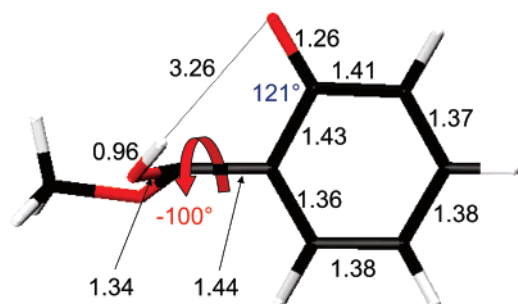


**Figure 8.** Selected geometric parameters (bond lengths in angstroms and angles in degrees) for methyl salicylate  $S_1/S_0$  MECI as determined by SA-2-CAS(2/2)-MSPT2/6-31G\*.

fluorescence maximum of 2.82 eV. This implies that the SA-2-CAS(2/2)-PT2 value for the Stokes shift is too large, assuming vertical absorption and emission transitions. As can be seen in Figure 2, the predicted fluorescence maximum from the AIMS dynamics occurs at higher energy than that predicted by this static calculation. This is because there is insufficient time for complete vibrational relaxation in the first 100 fs investigated here. Adjusting the  $C_2C_7O_2H$  and  $C_3C_2C_7O_2$  dihedral angles to make the molecule planar increases the  $S_0/S_1$  energy gap at this

$S_1$  keto minimum by 0.2 eV. This might be expected to be more representative of the observed fluorescence maximum since the transition dipole moment will be larger for planar geometries. Enlargement of the active space to include eight electrons in eight orbitals, that is, SA-2-CAS(8/8)-MSPT2, further increases the gap by a similar amount.

Finally, we have searched for an  $S_1/S_0$  minimal energy conical intersection (MECI) in order to rationalize the experimental observation that the fluorescence quantum yield decreases dramatically with increasing excitation energy.<sup>13,22,23</sup> We located this intersection using the multistate CASPT2 method,<sup>41</sup> as implemented in MolCas,<sup>42</sup> and a new algorithm we developed<sup>43</sup> for MECI optimization, which does not require nonadiabatic coupling vectors (which are not yet implemented for CASPT2). The resulting geometry is shown in Figure 8. The primary distortion leading from the  $S_1$  keto minimum to the  $S_1/S_0$  MECI is torsion about the  $C_2-C_7$  bond, which opens the chelate ring and leads to a loss of all H-bonding character. The importance of this twisting coordinate has been noted previously<sup>1,2</sup> for malonaldehyde, the paradigmatic ESIPT molecule corresponding to the chelate ring of MS. Interestingly, the resulting MECI is a three-state intersection for malonaldehyde, where the lowest-lying bright excited state is  $S_2$ . In MS, the bright excited state is  $S_1$ ; therefore, it is not surprising that this MECI is a conventional two-state intersection here. This MECI lies 0.48 eV above the keto  $S_1$  minimum, but we note that an intervening barrier is possible.

A detailed energy level diagram depicting all of the important stationary points is provided in Figure 9. Energy differences are shown using both the SA-2-CAS(2/2)-PT2 method used to determine the optimized geometries (normal text) and also CASPT2 with an enlarged active space, SA-2-CAS(8/8)-PT2 (italic text). The basic picture is not modified significantly by the enlargement of the active space. Both active spaces generate vertical excitation energies in close proximity to the experimental absorption maximum, correct to within roughly 0.2 eV (experimental values are given in bold). However, as noted above, the larger active space increases the  $S_1/S_0$  energy gap at

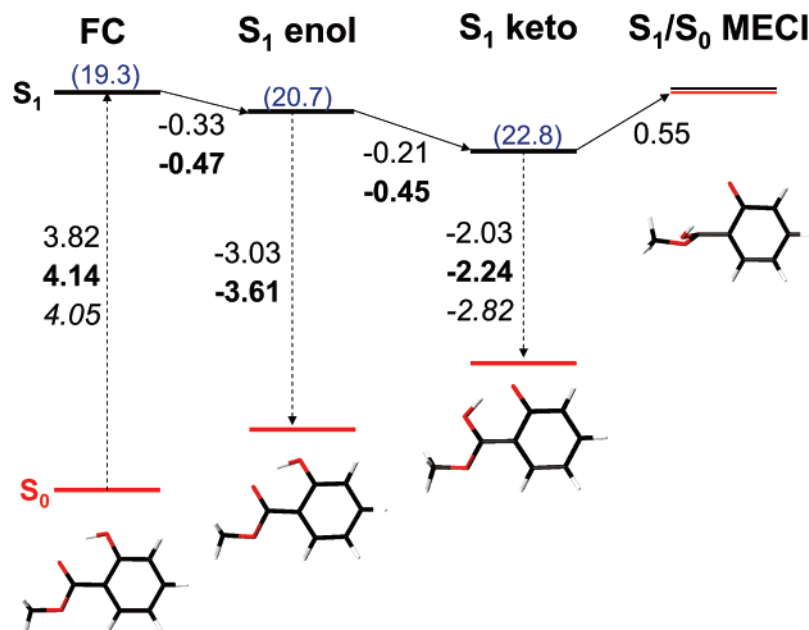


**Figure 9.** Energy level diagram of important geometries in methyl salicylate. Geometries are optimized with SA-2-CAS(2/2)-PT2/6-31G\* for minima and with SA-2-CAS(2/2)-MSPT2/6-31G\* for the  $S_0/S_1$  MECI. Energy differences (in electronvolts) are shown as calculated with SA-2-CAS(2/2)-PT2 (normal text) and SA-2-CAS(8/8)-PT2 (bold text). These are compared to experimental values (italic text), where available. The square norm of the  $S_0/S_1$  transition dipole moment (in Debye<sup>2</sup>) is shown in blue text in parentheses for the minima.



the  $S_1$  keto minimum such that it is in closer accord with the experimentally observed fluorescence maximum. Thus, it is likely that a combination of incomplete vibrational relaxation, enhanced fluorescence from planar geometries, and the need for a larger active space are all important in reconciling the theoretical prediction and experimental observation of the Stokes shift.

We wish to make two connections between CASPT2 energetics and that derived from experiment. The first is identification of the 0–0 transition reported in the literature with excitation to the local (enol)  $S_1$  minimum, not the global (keto)  $S_1$  minimum. This assertion is supported by the excellent agreement then obtained between theoretical and measured differences between vertical and adiabatic excitation energies, along with the more favorable Franck–Condon factor connecting the two enol geometries. We can also identify access to the twisted MECI as the relaxation channel responsible for the sudden falloff in fluorescence yield. Given excitation to the local enol minimum as the “origin” reported in previous literature, the energy required to reach the  $S_1/S_0$  MECI predicted by CASPT2 becomes  $\approx 2740\text{ cm}^{-1}$  (an error of  $<0.2\text{ eV}$ ), in comparison with the best experimental estimate for opening the efficient nonradiative decay pathway of  $1300\text{ cm}^{-1}$  obtained previously. As noted above, there may be a barrier between the  $S_1$  keto minimum and the  $S_1/S_0$  MECI shown in Figure 8. Further investigation of this point and calculation of the resulting decay rates as a function of excess excitation energy would be interesting as a test of this hypothesis. Note that similar proposals have recently been made for the closely related ESIPT molecules malonaldehyde<sup>1,2</sup> and salicylic acid.<sup>20</sup> Whereas rotamerization in malonaldehyde is barrierless and thus fast enough to sometimes preclude ESIPT entirely, slow (and energetically unfavorable) twisting in MS leads to a separation of timescales enabling isolation of each process. Rotamerization has been suggested before as being responsible for the threshold behavior,<sup>13</sup> and we have found similarly twisted  $S_1/S_0$  intersections in a number of other ESIPT molecules.<sup>44</sup>

## Summary and Conclusion

We have presented the first report of ab initio excited-state dynamics on a CASPT2 potential surface, in particular, for the ESIPT reaction in methyl salicylate. Perturbation corrections are essential to an accurate description of the process, in that spurious barriers predicted at the CASSCF level significantly hinder the reaction. AIMS simulations using the correlation-corrected potential make quantitatively correct predictions concerning the time scale for hydrogen atom transfer (fluorescence recovery). Static calculations performed at the same level of theory reveal ESIPT to be favorable only when preceded by bond alternation, the spectator modes serving as a “bath” that shifts relative minima of excited-state tautomers and thereby fashions a viable pathway for particle exchange. Motion of the wavepacket may be succinctly summarized as that of a knight in chess, an L-shape resulting in passive exchange of the light atom.

The driving force behind the reaction is the electronic reorganization accompanying excitation (see the HOMO and LUMO in Figure 1), creating a bond alternation pattern that favors tautomerization. Thus, it is probably preferable to say that the “electronic switching” referred to elsewhere<sup>16</sup> takes place upon excitation, not at the point of particle transfer. The ESIPT process is best viewed as excited-state relaxation, with the nuclei getting back “into sync” with the new, excited arrangement of electrons.

In conclusion, we have simulated ESIPT in MS using first-principles quantum dynamics accounting for both static and dynamic electron correlation. The lack of an isotope effect in ESIPT for MS is due to the dominance of a skeletal coordinate in the reaction. Quantitative agreement with femtosecond experiments demonstrates the accuracy of the AIMS-CASPT2 method. Development of analytic gradients and nonadiabatic coupling matrix elements within the multistate formulation<sup>41</sup> of CASPT2 is forthcoming. This will be a critical step toward modeling nonadiabatic transitions with AIMS-CASPT2.

**Acknowledgment.** The authors are pleased to acknowledge lively discussions on ESIPT with Professor A. Zewail. This work was supported by NSF CHE-02-311876 and CHE-05-35640.

**Supporting Information Available:** Cartesian coordinates of geometries discussed in the text. This material is available free of charge via the Internet at <http://pubs.acs.org>.

## References and Notes

- (1) Coe, J. D.; Martinez, T. J. *J. Phys. Chem. A* **2006**, *110*, 618.
- (2) Coe, J.; Martinez, T. J. *J. Am. Chem. Soc.* **2005**, *127*, 4560.
- (3) Sanchez-Galvez, A.; Hunt, P.; Robb, M. A.; Olivucci, M.; Vreven, T.; Schlegel, H. B. *J. Am. Chem. Soc.* **2000**, *122*, 2911.
- (4) Martinez, T. J. *Acc. Chem. Res.* **2006**, *39*, 119.
- (5) Ben-Nun, M.; Quenneville, J.; Martínez, T. J. *J. Phys. Chem. A* **2000**, *104*, 5161.
- (6) Doltsinis, N. L.; Marx, D. *Phys. Rev. Lett.* **2002**, *88*, 166402.
- (7) Roos, B. O. *Adv. Chem. Phys.* **1987**, *69*, 399.
- (8) Baeck, K. K.; Martinez, T. J. *Chem. Phys. Lett.* **2003**, *375*, 299.
- (9) Roos, B. O. *Acc. Chem. Res.* **1999**, *32*, 137.
- (10) Celani, P.; Werner, H.-J. *J. Chem. Phys.* **2003**, *119*, 5044.
- (11) Tsien, R. Y. *Annu. Rev. Biochem.* **1998**, *67*, 509.
- (12) Chattoraj, M.; King, B. A.; Bubltz, G. U.; Boxer, S. G. *Proc. Natl. Acad. Sci. U.S.A.* **1996**, *93*, 8362.
- (13) Herek, J. L.; Pedersen, S.; Banares, L.; Zewail, A. H. *J. Chem. Phys.* **1992**, *97*, 9046.
- (14) Douhal, A.; Lahmani, F.; Zewail, A. H. *Chem. Phys. Lett.* **1996**, *207*, 477.
- (15) Lochbrunner, S.; Schultz, T.; Schmitt, M.; Shaffer, J. P.; Zgierski, M. Z.; Stolow, A. *J. Chem. Phys.* **2001**, *114*, 2519.
- (16) Lochbrunner, S.; Wurzer, A. J.; Riedle, E. *J. Phys. Chem. A* **2003**, *107*, 10580.
- (17) Tanner, C.; Manca, C.; Leutwyler, S. *Science* **2003**, *302*, 1736.
- (18) Schmidtke, S. J.; Underwood, D. F.; Blank, D. A. *J. Am. Chem. Soc.* **2004**, *126*, 8260.
- (19) Aquino, A. J. A.; Lischka, H.; Hattig, C. *J. Phys. Chem. A* **2005**, *109*, 3201.
- (20) Sobolewski, A. L.; Domcke, W. *Phys. Chem. Chem. Phys.* **2006**, *8*, 3410.
- (21) deVivie-Riedle, R.; DeWaele, V.; Kurtz, L.; Riedle, E. *J. Phys. Chem. A* **2003**, *107*, 10591.
- (22) Felker, P. M.; Lambert, W. R.; Zewail, A. H. *J. Chem. Phys.* **1982**, *77*, 1603.
- (23) Smith, K. K.; Kaufmann, K. J. *J. Phys. Chem.* **1978**, *82*, 2286.
- (24) Scheiner, S. J. *J. Phys. Chem. A* **2000**, *104*, 5898.
- (25) Sobolewski, A. L.; Domcke, W. *Chem. Phys. Lett.* **1999**, *300*, 533.
- (26) Peteanu, L. A.; Mathies, R. A. *J. Phys. Chem.* **1992**, *96*, 6910.
- (27) Chudoba, C.; Riedle, E.; Pfeiffer, M.; Elsaesser, T. *Chem. Phys. Lett.* **1996**, *263*, 622.
- (28) Lochbrunner, S.; Szeghalmi, A.; Stock, K.; Schmitt, M. *J. Chem. Phys.* **2005**, *122*, 244315.
- (29) Takeuchi, S.; Tahara, T. *J. Phys. Chem. A* **2005**, *109*, 10199.
- (30) Ben-Nun, M.; Martínez, T. J. *J. Chem. Phys.* **1998**, *108*, 7244.
- (31) Ben-Nun, M.; Martinez, T. J. *Adv. Chem. Phys.* **2002**, *121*, 439.
- (32) Heller, E. J. *J. Chem. Phys.* **1981**, *75*, 2923.
- (33) Werner, H.-J. *Mol. Phys.* **1996**, *89*, 645.
- (34) Celani, P.; Werner, H.-J. *J. Chem. Phys.* **2000**, *112*, 5546.
- (35) Werner, H.-J.; Knowles, P. J.; Lindh, R.; Schütz, M.; Celani, P.; Korona, T.; Rauhut, G.; Amos, R. D.; Bernhardsson, A.; Berning, A.; Cooper, D. L.; Deegan, M. J. O.; Dobbyn, A. J.; Eckert, F.; Hampel, C.; Hetzer, G.; Lloyd, A. W.; McNicholas, S. J.; Meyer, W.; Mura, M. E.; Nicklass, A.; Palmieri, P.; Pitzer, R.; Schumann, U.; Stoll, H.; Stone, A. J.; Tarroni, R.; Thorsteinsson, T. *MOLPRO 2002.10*; a package of ab initio programs; see <http://www.molpro.net>.
- (36) Hehre, W. J.; Ditchfield, R.; Pople, J. A. *J. Chem. Phys.* **1972**, *56*, 2257.

(37) Hillery, M.; O'Connell, R. F.; Scully, M. O.; Wigner, E. P. *Phys. Rep.* **1984**, 106, 121.

(38) Subsequently, we have compared the B3LYP geometry with that optimized using SA-2-CAS(2/2)-PT2 (see Figures S3 and S4 in the Supporting Information), and there is no discernable difference.

(39) Zgrablić, G.; Voitchovsky, K.; Kindermann, M.; Haacke, S.; Chergui, M. *Biophys. J.* **2005**, 88, 2779.

(40) Helmbrook, L. H.; Kenny, J. E.; Kohler, B. E.; Scott, G. W. *J. Phys. Chem.* **1983**, 87, 280.

(41) Finley, J.; Malmqvist, P.; Roos, B. O.; Serrano-Andres, L. *Chem. Phys. Lett.* **1998**, 288, 299.

(42) Karlstrom, G.; Lindh, R.; Malmqvist, P.-A.; Roos, B. O.; Ryde, U.; Veryazov, V.; Widmark, P.-O.; Cossi, M.; Schimmelpfennig, B.; Neogady, P.; Seijo, L. *Comput. Mater. Sci.* **2003**, 28, 222.

(43) Levine, B. G.; Ko, C.; Quenneville, J.; Martinez, T. J. *Mol. Phys.* **2006**, 104, 1053.

(44) Coe, J. D.; Martinez, T. J. Unpublished results.